Simulation Study of Spectral Absorption Lengths in Seawater using ^{40}K Decay

Bachelorarbeit aus der Physik

Vorgelegt von
Johannes Schumann
20. Februar 2018

Friedrich-Alexander-Universität Erlangen-Nürnberg

Betreuer: Prof. Dr. Ulrich Katz

Abstract

The neutrino telescope KM3NeT is a neutrino detector currently being built for the research on astrophysical neutrinos and the determinantion of the neutrino mass hierarchy. The detector is sensitive to the visible regime of the Cherenkov light, and will fill out a volume of several cubic kilometres in the deep Mediterranean Sea, which makes the sea water an important part of the experiment.
Thus, the knowledge about the optical properties of this enviroment is important for the precise analysis of the data. An important optical property, the absorption length of the water, can vary for example the sea current causing a changed water composition.
In this study the idea of using the natural occuring potassium 40 (^{40}K) in the sea water and different colour filters to monitor the absorption length is evaluated based on a computer simulation.

Zusammenfassung

Das im Aufbau befindliche Neutrinoteleskop KM3NeT, ist ein Teleskop mit dem zukünftig astrophysikalische Neutrinos und die Neutrinomassenhierarchie untersucht werden sollen. Namensgebend für das Projekt ist das Volumen von mehreren Kubikkilometern, welches von dem Detektor, durch die Platzierung der einzelnen Bestandteile in der Tiefsee des Mittelmeeres, aufgespannt werden wird.
Dieser Standort abseits einer kontrollierten Laborumgebung macht es notwendig, die sich veränderten Umweltbedingungen im Blick zu behalten, damit die Messergebnisse richtig interpretiert werden können. Ein wichtiger Punkt dabei sind die optischen Eigenschaften und im speziellen die Absorptionslänge des Meerwassers, welche sich, z.B. durch eine mittels Strömung variierende Zusammensetzung, ändern können.
Eine Idee, um diese Absorptionslänge zu Überwachen, ist die Messung des Lichtuntergrunds durch den natürlichen Kalium 40 (^{40}K) Zerfall mittels einiger mit Filtern modifizierter optischer Module. Diese Möglichkeit soll in dieser Arbeit anhand von Simulationsdaten untersucht werden.

Contents

1 Introduction

In 1912, Victor Hess discovered the cosmic radiation, which is, for the most part, the flux of charged particles from galactic and extragalactic sources. This discovery can be seen as the last centuries analogon of the gravitational waves detection in 2016 and set the starting point for the research field of astroparticle physics.
A problem of charged particles as cosmic messengers is, that they are deflected by electromagnetic fields, which complicates the identification of their glactic or extragalactic point sources. Since they are uncharged and thus not deflected by magnetic fields, neutrinos are an excellent cosmic messenger. In addition, neutrinos only interact via the weak force in the standard model of particle physics and can thus escape dense sources and are seldom absorbed by matter on their way to Earth. This weak interaction makes them extremely difficult to detect and, further on, large detector volumes necessary. A famous picture that stands for this need for large volumes is the cleaning scene of photomultipliers with a boat at the Kamiokande experiement. This experiment has a volume of $3 \cdot 10^{-7}\,\mathrm{km}^3$, which is a huge effort to provide as a controlled environment and is still just a fraction for what is needed to do neutrino astronomy. Therefore neutrino telescopes are placed in a natural enviroment within the required optical properties. In the deep sea of the Mediterranean, where the KM3NeT detector is located, these optical properties can vary in a certain range, for example due to sea current changing the water composition.
In this bachelor thesis the idea of monitoring the absorption length of the seawater using the spectral separated detection of ^{40}K coincidences is studied. A hardware solution for this ansatz would require some digital optical modules (DOM) to be equipped with color filters in front of the photomultiplier tubes (PMTs). On the one side, this is more expensive, and on the other side the effective photosensitive area of the modified DOMs decreases. Thus, the gathered advantage of a well known absorption length has to be evaluated very carefully to compensate the disadvantages.

2 Physical Basics

This chapter recapitulates the main physical principles, which are essential for the idea of this study.

2.1 Optical Properties of Seawater

Seawater is an almost homogenous dielectric material, thus the light propagates without sigificant influence of interference. Therefore the optics can be seen as the propagation of whole wave packages. For this photon particle picture the processes of absorption and scattering have to be characterised. Both effects depend on the distance the photon has travelled and are described by an exponential law. So the absorption length $L(\lambda)$ and the scattering length[1] $S(\lambda)$ are defined as the distance, when $\propto e^{-1}$ of the initial photons (N_0 at $d = 0$) are absorbed or scattered. The amount of not-absorbed photons N_{abs} after a distance d is therefore given by

$$N_{\text{abs}} = N_0 \exp\left(-\frac{d}{L(\lambda)}\right) \ , \tag{2.1}$$

and similarly for the scattered photons N_{scat}

$$N_{\text{scat}} = N_0 \exp\left(-\frac{d}{S(\lambda)}\right) \ . \tag{2.2}$$

After a photon has been scattered it still accounts to the visible spectrum, which makes the information about the subsequent direction important. This information is encoded in the parameter $p(\theta, \lambda)$, the probability of a photon of wavelength λ to be scattered under the angle θ.

In order to give meaningful results in the end of this study, the KM3NeT water model was used as value basis for these three parameters [int14]. This data is plotted in Figure 2.1 and 2.2.

[1] This scattering length is not connected to the definiton of the effective cross section in the limit of $k \to 0$.

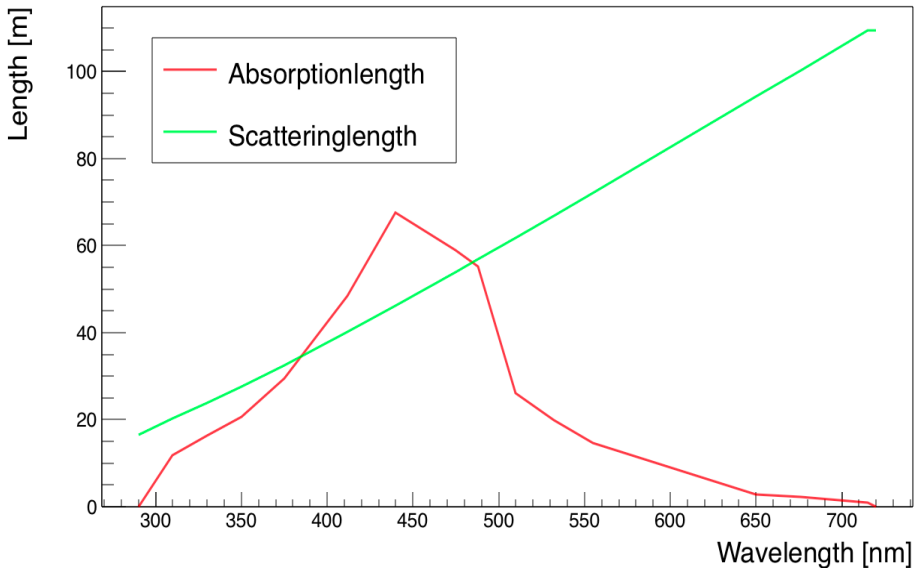

Figure 2.1: Absorption and scattering length as a function of the wavelength, describing the water properties in the KM3NeT water model [int14].

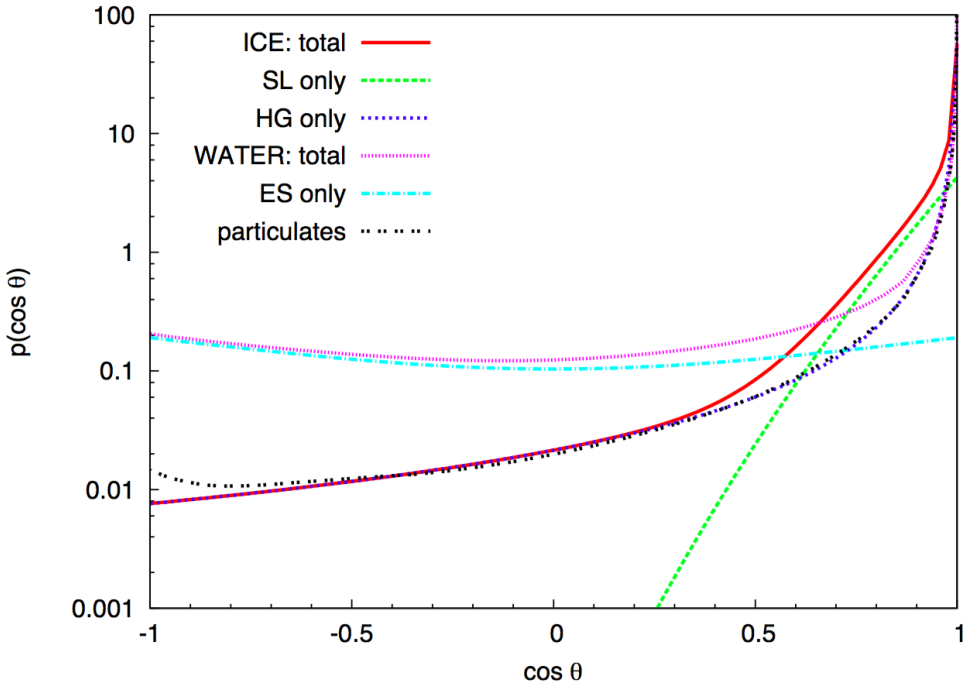

Figure 2.2: Scattering probability for an exemplary wavelength of 400 nm. The dashed pink line refers to the seawater. Figure taken from [JH15].

2.2 Potassium 40 (^{40}K)

The isotope $^{40}_{19}$K (potassium-40) has a natural occurence of about $0,012\%$, so its decay constitutes a large portion of the natural radioactivity [Nie50]. The following values are according to [url18b]. This isotope has a half-life of $\tau = 1.28 \cdot 10^9$y $(4.0 \cdot 10^{25}$ns) and the decay can happen via three processes. With a percentage of 0.001%, the least probable one is the β^+-decay

$$^{40}_{19}\mathrm{K} \longrightarrow {}^{40}_{18}\mathrm{Ar} \ + \ e^+ \ + \ \nu_e \ .$$

The free positron will directly disappear through annihilation, which emits two photons with an energy of at least the rest mass of the electron, each. This energy of 511keV lies in the gamma regime. The second most occuring decay process is the electron capture, which occurs in 10.72% of the cases and is given by

$$^{40}_{19}\mathrm{K} + e^- \longrightarrow {}^{40}_{18}\mathrm{Ar} \ + \ \nu_e \ + \ \gamma \ .$$

The electromagnetic waves, which are emitted by the electron capture, are in the gamma regime, too. In most of the cases (89.28%) a ^{40}K atom decays via β^--decay

$$^{40}_{19}\mathrm{K} \longrightarrow {}^{40}_{20}\mathrm{Ca} \ + \ e^- \ + \ \bar{\nu}_e \ .$$

The transition energy of this process is 1.33MeV, which is divided in the masses of the electron and the neutrino, as well as in the kinetic energies. So the maxium kinetic energy an electron from this process can have is

$$\begin{aligned} \max(E_{\mathrm{kin}}) &= E_{\mathrm{transition}} - E_0 && (2.3) \\ &= 1.33\,\mathrm{MeV} - 0.511\,\mathrm{MeV} = 0.819\,\mathrm{MeV} \ . && (2.4) \end{aligned}$$

The β^--decay is the most important process for this study, because the electron emits light by Cherenkov radiation (see Section 2.3). Due to the optical properties of the seawater, most importantly being transparent in the visible regime, a significant part of the Cherenkov spectrum can be detected by the photo sensors.

According to the information from the ANTARES project, the activity of ^{40}K in the seawater is about $A_K = 13,750 \frac{\mathrm{Bq}}{\mathrm{m}^3}$ [Bru99].

2.3 Cherenkov Radiation

A charged particle moving through a dielectric medium, with a speed faster than the phase velocity of light in the material, causes the emission of Cherenkov radiation. In the huygens picture, a spherical wave is emitted from each point of the track. For the considered fast particle, these waves produce a Mach cone, in this specific context called the Cherenkov cone.

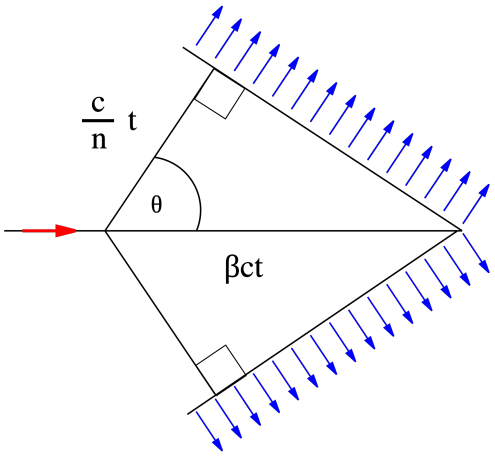

Figure 2.3: Visualisation of the Cherenkov cone geometry including the formula expression for the cone dimensions. The red arrow points in the direction of the charged particle momentum and the blue arrows towards the propagation direction of the Cherenkov light. Figure taken from [Hor06].

In the ^{40}K case, the geometry of the light source based on the Cherenkov cone can be neglected. As it is well know, e.g. from teaching in high school, the β^--radiation can be shielded only using a thin layer of aluminium, which gives an idea of the size of such a light emitting track. The decrease of energy over the track length in a certain material is linear with the current energy of the particle, which yields,

$$\frac{\mathrm{d}E}{\mathrm{d}x} = -\frac{1}{d}E(x) \tag{2.5}$$

$$\Rightarrow \qquad E(x) \propto \exp\left(-\frac{x}{d}\right) \ , \tag{2.6}$$

with d called the inelastic mean free path. For water and electrons with energies around 1 MeV, this inelastic mean free path is less than a centimetre, which makes it approximately pointlike in the given context.

For doing spectral studies, the knowledge of the emitted wavelength distribution from Cherenkov radiation is important. It is given by the Tamm-Frank-Formula [FB92]

$$\frac{\mathrm{d}E}{\mathrm{d}x} = \frac{e^2}{c^2} \int \left(1 - \frac{1}{n^2\beta^2}\right) \omega \, \mathrm{d}\omega \ , \tag{2.7}$$

which can be reshaped according to [Her17, B.1] in the form

$$\frac{\mathrm{d}E}{\mathrm{d}x} = 4\pi^2 e^2 \int \left(1 - \frac{1}{n^2\beta^2}\right) \frac{1}{\lambda^3} \, \mathrm{d}\lambda \ . \tag{2.8}$$

The refractive index of the water is known in the visible range with being about $n \approx 1.33$. For relativistic particles of $\beta \approx 1$, the expression in the brackets is wavelength independent. This means the distribution of visible Cherenkov radiation is $S(\lambda) \propto \frac{1}{\lambda^2}$.

2.4 Photomultiplier Tubes

A photomultiplier tube (PMT) is a device for detecting light of weak intensity, even down to a single photon. The most common construction for those is an evacuated vacuum tube with a photocathode at its front (Figure 2.4). An incoming photon has a chance to release an electron from the cathode via the photoelectric effect. The probability of this happening is called quantum efficiency (QE) and can be determined for each PMT individually (Figure 2.5). By applying gradationally increasing

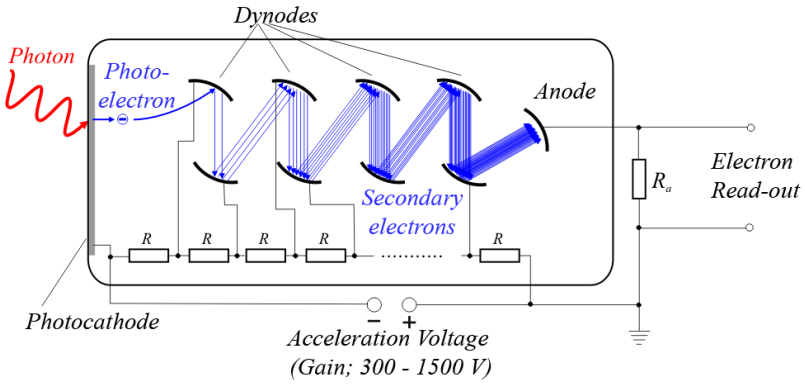

Figure 2.4: Schematic drawing of a photomultiplier tube (PMT). Figure taken from [Kri14].

high voltages at the dynodes, electric fields are generated between the photocathode and the dynodes, thus the electron is accelerated towards the first dynode and between the dynodes. The portion of accelerated electrons, which hit the first dynode,

is given by the so called collection efficiency (CE). For the Hamamatsu R12199-02 (currently used as photo detector in the KM3NeT detector) the CE is about 90%. An electron hitting the first dynode releases a number of electrons given by the secondary emission coefficient upon the impact. These are accelerated towards the next dynode. This process is repeated until the electron cascade results in a measurable current at the anode.

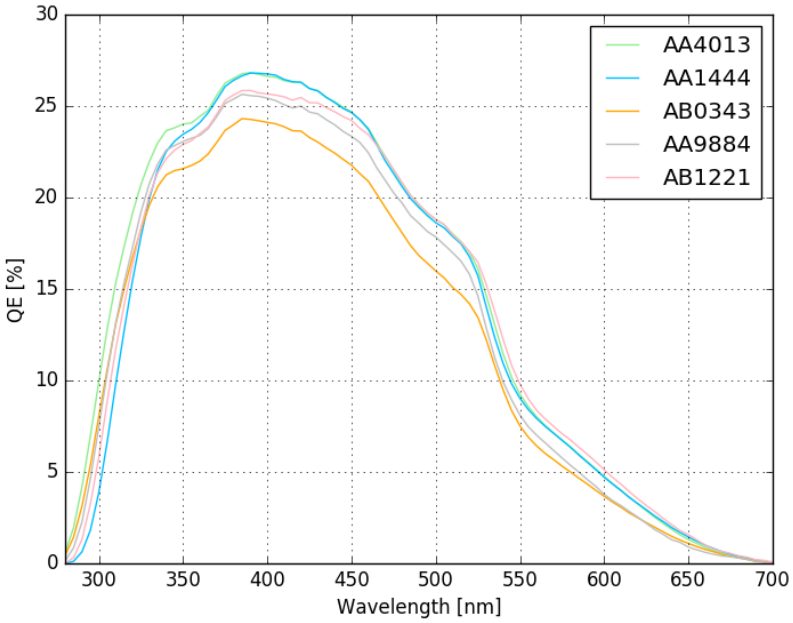

Figure 2.5: Measured quantum efficiency for five PMTs of type Hamamatsu R12199-02, which is used in the KM3NeT project.

3 Neutrino Astronomy and KM3NeT

This study is done for the neutrino telescope KM3NeT, which is currently constructed at two sites in the Mediterranean Sea. To convey an idea about the basic concepts and parameters, a brief overview about neutrino astronomy and the project will be given in the following.

3.1 Neutrino Detection

Neutrinos are very light uncharged particles in the standard model, which are only interacting in terms of the electroweak interaction. Therefore these particles can only be detected indirectly, after a neutrino has passed part of its energy to a charged particles. The related weak interaction processes via $W^{\pm}$ or Z^0 bosons are given as Feynman diagrams in Figure 3.1. In the observed energy range the secondary

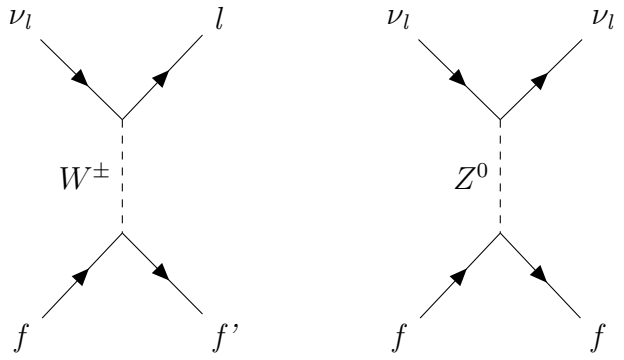

Figure 3.1: Feynman diagrams for neutrino-fermion scattering for charged (left) and uncharged (right) current and lepton family l. Figure taken from [Hof17, fig 2.2].

particles produces Cherenkov radiation in the dielectric medium the detector consists of. Via the Cherenkov light signature, the direction and the energy of the primary neutrino can be reconstructed.

3.2 The KM3NeT Digital Optical Module

In order to fulfil the requirement of optical monitoring a large volume, neutrino telescopes are assembled as a large array of optical sensor units, which are regularly arranged all over the volume. Such an optical sensor, called digital optical module (DOM), houses the detection devices, e.g. PMTs and auxiliary electronics, in order to provide the detection data as digitised signals.

The used design for the KM3NeT detector is based on a 17 inch glass sphere, with its detection area split up into 31 single PMTs, resulting in an improved angular resolution and overall photocathode area compared to conventional single PMT optical modules. The area of the DOM available for placing detection devices, is limited

(a) Real KM3NeT-DOM including connector and mechanical mounting. Image taken from [url18a].

(b) Simulated KM3NeT-DOM.

Figure 3.2: Comparison between the real and simulated digital optical module.

at the top half sphere due to the mushroom shaped aluminum cooling device which also houses the penetrator responsible for the transmission of power and signal data. As can be seen in Figure 3.2 the lower half sphere has additional 7 PMTs. It is a wise decision to "waste" the space on the top, because of the larger interest in events coming from the seafloor upwards, which have a less proportion of neutrinos from atmospheric events, which are considered as background for the detection of cosmic neutrinos.

For a possible hardware solution of this studies topic, different filters could be placed in front of the PMTs. The angular orientation of the filters does not matter, because the ^{40}K is equally distributed in the seawater. Only close-by PMTs should be used

for the same filter, due to the higher coincidence rates at small angles between the PMTs.

3.3 KM3NeT Design

The description in this section follows maily the KM3NeT letter of intent [AM16].

In KM3NeT 18 DOMs comprise a so-called string. These vertical structures are anchored at the seafloor and pulled straight upwards by buoys. In order to cover the desired volume, multiple of these strings are placed in regular distances to each other. An artwork of such a setup is given in Figure 3.3. KM3NeT is developed to

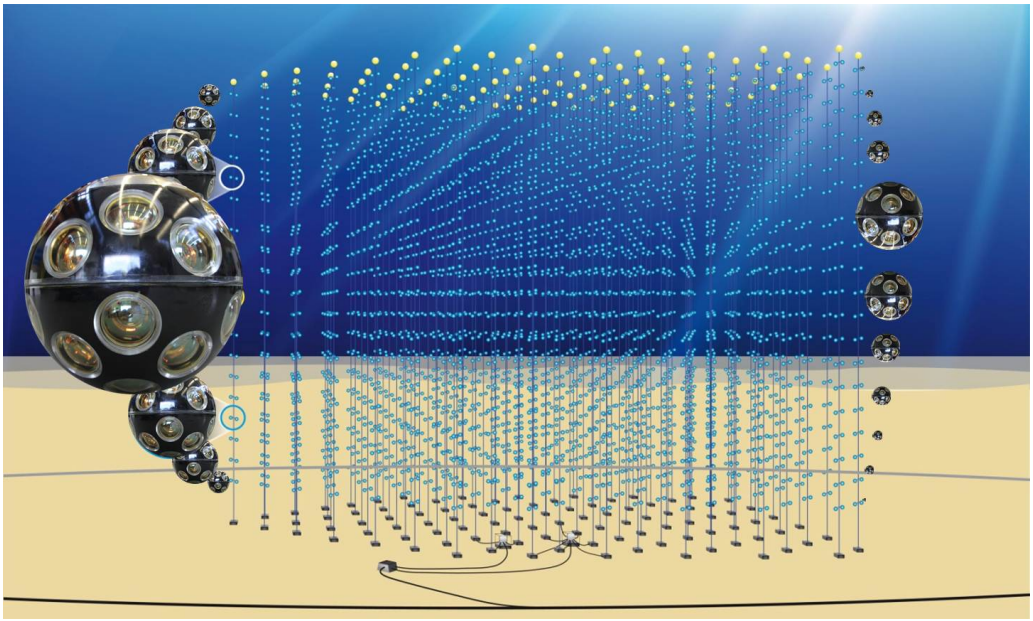

Figure 3.3: Artwork of a KM3NeT building block [url18a].

study multiple open scientific questions. Therefore the detector is split up into two subdetectors.

ORCA (Oscillation Research with Cosmics in the Abyss) is mainly designed for the research on the neutrino mass hierarchy. It is located roughly 40 km off the French coast near Toulon in the Meditteranean Sea and covers an instrumented volume of $7 \cdot 10^{-3}\,\mathrm{km}^3$ in a depth of about 2400 m. This corresponds to 115 vertical strings with 18 DOMs each and a vertical distance of 9 m between the DOMs and a inter-string spacing of 9 m, where the first DOM is 40 m above the seafloor.

ARCA (Astroparticle Research with Cosmics in the Abyss) is primarily designed for detecting very-high energetic neutrinos. It is located roughly 100 km off the Italian

coast near Portopalo di Capo Passero and also has 115 vertical strings covering a detector volume of $0.5\,\mathrm{km}^3$, which means that the horizontal and vertical spacing between the DOMs is increased.

With version KM3NeT2.0, the detector volume will be increased to its strived final size of several cubic kilometres.

4 Simulation enviroment

The simulation implementation *nuke4* was adopted from Björn Herold, who programmed it for his studies within his PhD thesis titled "Simulation and Measurement of Optical Background in the Deep Sea Using a Multi-PMT Optical Module" [Her17]. He studied the effects of ^{40}K as optical background for deep-sea neutrino telescopes. Within the scope of this work, the available tools were further developed and adapted to the problem of using the spectral information of the measured K40 photons to study the absorption length of seawater.

4.1 GEANT4

The simulation is based on the GEANT4 framework, which stands for "**Ge**ometry **an**d **T**racking" in its fourth version. It is an open-source particle physics simulation enviroment developed at CERN (European Organization for Nuclear Research). The employed programming language in this current version is C++, after it has been FORTRAN until GEANT3 [url17].

The most important part when setting up a GEANT4 simulation is the instance of the `G4RunManager`-class, which does all the needed initializations and controls of the simulation. All relevant customisations are done by the derivation of predefined abstract classes, which are passed to the `G4RunManager` by calling the method `SetUserInitialization`. The most important of these abstract classes for the used implementation are:

- `G4VUserDetectorConstruction`

  This class contains the detector geometry, as well as the associated materials including their properties, e.g. surface finish, material composition, scattering properties, etc.

- `G4VUserPhysicsList`

  The simulated physical processes and interactions are defined in the class `G4VUserPhysicsList`. Examples are strong, weak, electromagnetic interaction or effects like Compton or Reyleigh scattering.

- `G4UserSteppingAction`

  The possibility of taking custom actions between each simulation step is given by this class type. In the *nuke4* simulation it is used to store the information about photons arriving at the photocathode material. A photon is also removed from the simulation after hitting the photocathode. The physical processes in the PMT leading to the signal amplification are not considered within the main simulation.

The main disadvantage of the broad and detailed functionality is the long run time of GEANT4 simulations compared to others frameworks. As a consequence, physics processes happening inside the PMT, like the amplification of the signal in the dynode system, are not simulated. Their average effect are taken into account afterwards based on the photon information (see Section 4.4).

4.2 GEANT4 Geometry

The GEANT4 geometry describes the spatial structure and the physical material characteristics of the simulated setup. It is composed of several single volumes, of which the largest one is called "world". All other parts are contained in this world and all actions of the simulation are limited to it. If all simulated particles have left this world volume the setup is at rest and a single run is finished.

In order to define a volume, a `G4VSolid` object is initialised, defining its shape. Several shapes are predefined by derivatives of `G4VSolid`, e.g. `G4VElipsoid`. After the initialisation of the basic shape, a logical volume (`G4VLogicalVolume`) has to be created, which gives the object physical properties. This transformation from a geometrical shape to an object consisting of a certain material is described in detail in Section 4.2.2. The last step is to place the object into another parent volume (except the world volume), which is done by using an instance of `G4VPhysicalVolume`.

In the used setup, the world volume is a sphere equipped with the known material composition and the optical properties of the seawater, introduced in Section 2.1. The comparison of the effect of different absorption lengths is dealt with in detail along Chapter 5.

4.2.1 Detector Construction

The detector for the simulations consists of a single DOM positioned in the centre of the world volume. A comparison between a real KM3NeT DOM and its simulated geometry is given in Figure 3.2. A model of the DOM was already implemented in the *nuke4* code, but it had to be updated to the latest dimensions according to the

official KM3NeT blueprints.

In Figure 4.1 a sectional top view of the simulated design is given. The most important difference between the real and the simulated DOM is the shape of the support structure. In the real DOM, the support structure holds the PMTs in place mechanically and has thus a complex geometrical shape. In the simulation, a sphere shaped black foam with cylindrical cutouts is used as photon absorber, emulating only the optical properties of the support structure.

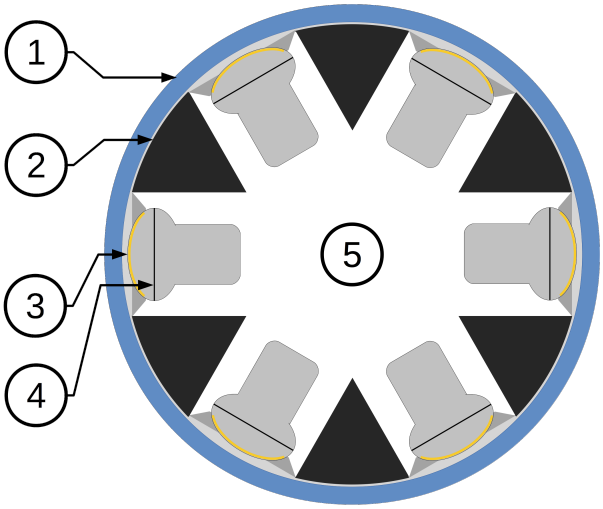

Figure 4.1: DOM structure as used in the simulation. Components: glass sphere (1), support structure made of foam material (2), PMT front with photocathode material (3), PMT absorber plate (4) and empty inner space from cylindric cutouts (5).

As mentioned previously, the PMTs in the simulation are not fully equipped with its inner structure, e.g. the dynode system. Just the glass body and the photocathode material are used. A component, which is not part of the original PMT design, is the absorber plate positioned at the widest point of each PMTs head ellipsoid. This absorber plate prevents photons from hitting the photocathode of a PMT on the opposite site of the DOM.

4.2.2 Material & Surface Properties

The definition of a material is done by an instance of the `G4Material` object, which can be passed to multiple instances of `G4VLogicalVolume` later on.
Such a material can be defined by its proportional composition of elements, molecules and other materials, using the `AddMaterial()` method. The GEANT4 framework

provides a broad library of the most common fundamental materials, e.g. elements (`G4Element`) or isotopes (`G4Isotopes`).
If a specific property is known, e.g. from measurement, the material behaviour can be set manually. This is done via the `AddProperty()` method and is used for seawater material in *nuke4* for setting the refractive index, the absorption length and the scattering length according to the available seawater data.

The definition of surface properties is done in a similar way as it was done for the materials via the `G4OpticalSurface` class. The most important of those properties are the simulation model, the type and the surface finish. The surface properties define the physical behavior of the boundary between two materials, thus it can not be treated like a `G4VLogicalVolume`, but as a composition of two volumes and its surface transition.
For this purpose the `G4LogicalBorderSurface` class is used, which is created from the surface information in the `G4OpticalSurface` instance, the primary and the secondary `G4VPhysicalVolume`.

4.3 Particle Sources & Configurations

A particle source provides the simulation environment with all kinds of particles. Those particles can be placed at any position in the simulated world. The information about the desired source configuration is passed to the compiled GEANT4 program through its command line. That makes sure that minor changes can be applied without changing the code and compiling it again.

4.3.1 White Quasi Laser

The first kind of particle source, used for the characterisation of the simulation behavior of the prepared geometry, is comparable to a perfect white laser with a small beam diameter. In the simulation photons are emitted from a square with a side length of 1μm and their momentum directions are parallel to the surface normal. These photons are equally distributed in the visible energy range between 1.5 eV and 4.5 eV, corresponding to 830 nm and 280 nm.

In the first configuration, this source was aligned with the center of the DOM in a distance of 1 m to 99 m. At the same time either the absorption length or the scattering length was set to infinity, so that the respective alternative one could be characterised. When characterising the scattering length, the momentum change for the photon at the scattering process was recorded, too. In this configuration the photons were recorded when arriving at the glass, to exclude effects from the

propagation through the glas and the gel layer.

The second application for this particle source is the investigation of the reflecting behaviour of the reflector ring around the PMT. For this purpose the source is placed right in front of the glass, aligned with an angle θ to the normal vector of the PMT and a displacement d with respect to the inner rim (see Figure 4.2).

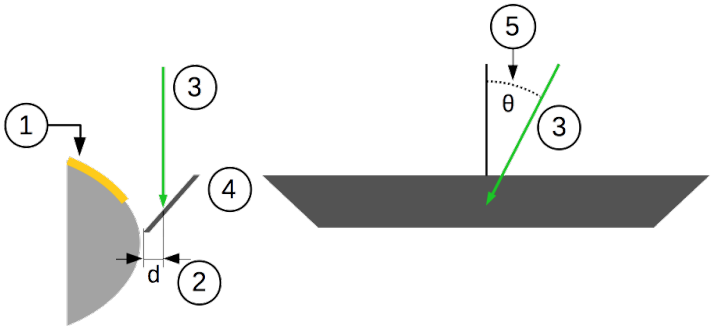

(a) Lateral view on the setup form two sides. Parts: PMT front (1), displacement d of the beam (2), beam (3), reflector ring (4) and beam angle to the PMT normal (5).

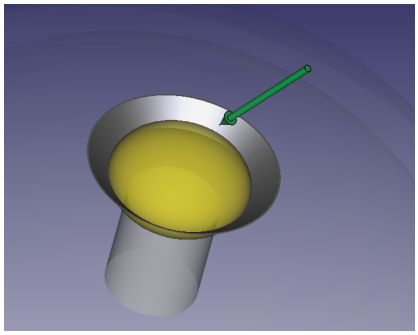

(b) 3D illustration of the setup. The green arrow shows the pointing of the light source.

Figure 4.2: Reflector ring test setup for the characterisation of the reflecting behavior in the simulation.

4.3.2 ^{40}K Decay

The simulated ^{40}K atoms are placed homogeniously in the world volume and being at rest in the world reference frame.

A technical problem arises from the rather large half-life of the ^{40}K isotope. Because a float point variable in double precision can handle only $2^{64} = 1.84 \cdot 10^{19}$ numbers and for the timestamps of photon events a resolution of nanoseconds is required, which would need a bit width of at least

$$b = \lfloor \log_2(4.0 \cdot 10^{25}) \rfloor + 1 = 86 \ . \tag{4.1}$$

The half-life values for every known isotope are listed in the `ENSDFSTATE.dat` file of GEANT4. In that file the value is set to zero. Therefore the timing in the simulation is not longer just given by the GEANT4 timestamp. Using the known activity A of ^{40}K in seawater, the total time elapsed T of the simulation can be calculated

afterwards with

$$T_{\text{sim}} = \frac{N}{V \cdot A} \ , \tag{4.2}$$

where V is the volume of the spheric world and N the number of decayed ^{40}K atoms. The total time for a received photon hit is therefore

$$t_{\text{recv}} = T_{\text{sim}} + t_{\text{run}} \ , \tag{4.3}$$

where t_{run} is the current time of the single run, which starts right after the ^{40}K is placed. The timing value t_{recv} gives the receive time of the photon with respect to the total simulation time. With the half-life being zero, this is equal to the time since the ^{40}K has been decayed.

4.4 Simulation Output

Since the amplification process inside the PMTs is not simulated, the simulation result always refers to the number of photons converted to photoelectrons at the photocathode. These and the used simulation parameters are written to text files, so they can be easily reviewed by eye. The Table 4.1 provides a list of the details stored for each recorded hit.

Property	**Description**	**Unit**
Event ID	Number of the simulation run equal to number of placed ^{40}K.	1
Hit time	Total time since the ^{40}K atom has been placed.	ns
Flight time	Time elapsed since the decay of the ^{40}K atom.	ns
Track length	Total tracklength of the photon.	m
Energy	Energy the photon is carrying	eV.
DOM ID	ID of the DOM, the involved PMT is located in.	1
PMT ID	ID of the PMT the photon has hit.	1
Event distance	Distance between the hit and the ^{40}K position.	m
Photon position	The position where the hit has happend.	m (coord.)
Photon direction	Unit vector in momentum direction the photon had before the hit.	$\lvert\vec{p}\rvert$=1

Table 4.1: Summary of informations about the simulated photons arriving at any of the photocathodes.

5 Simulation Data Analysis

5.1 Detection Rates

A detection rate ν is the number of occured events n within a period t, meaning

$$\nu = \frac{n}{t} \, . \tag{5.1}$$

The detection rate due a certain event type is the main quantity for the analysis of the detector data. The simulation data is also analysed in terms of detection rates, which makes the results directly compareable.

The most important types of rates are:

- **Darkrate:**
  The darkrate is the rate of PMT events, which occur without being caused by incident photons at the DOM surface. As the PMTs in the simulation are not equiped with their inner dynode structure, this effect is also not part of the simulation. It is considered in the analysis based on measurement experience. The darkrate for a single PMT is assumed as

  $$\nu_{\text{dark}} = 300\,\text{Hz} \pm 30\,\text{Hz}. \tag{5.2}$$

- **Background rate:**
  The background rate is the overall rate of PMT events not caused by a ^{40}K decay. It is composed of the darkrate and other received photons e.g. from bioluminesence activity.

- **Coincidence rate:**
  The rate of signals being detected at least at two PMTs within the coincidence time window of $\tau = 10\,\text{ns}$. The coincidence events can be correlated, e.g. from the same decay of a ^{40}K atom, or uncorrelated. An uncorrelated coincidence is also called random coincidence and can be caused for example from two different ^{40}K decays. The coincidence rates are categorised to their order which

is basically the number of received hits within the coincidence time window.

- **Single-hit rate:**
  The rate of a single-hit received at the PMTs within the coincidence time window. In terms of the coincidence-order classification, the single rates are the coincidence rates of order 1.

The detector is monitoring time dependent rates, which is done via evaluating timeslices of 0.1 s which yields a update frequency for the rates of 10 Hz. For the simulation the situation is a different one, because the total "measurement" time T_{sim} is in the order of one timeslice duration, but the enviromental conditions in the simulation are constant. Thus, no time dependent rates are calculated, which means $t = T_{\text{Sim}}$.

5.1.1 Simulation Detection Rates

In general, the situation for the simulation data is a different one than for the detector data, because even though the "measurement" time is very short, the whole situation at the photocathode is known. Therefore, a photon does not account just as one event if it is detected, but every photon hitting the photocathode material contributes to the total event number n with a certain weight w. This weight is always calculated for a coincidence time window in several steps.

First, all photon hits are split up in disjunct groups covering a coincidence timespan of $\tau = 10\,\text{ns}$ each. If each involved PMT gets just one hit of a photon with wavelength λ, the detection probabiltiy is just

$$p(\lambda) = \text{CE} \cdot \text{QE}(\lambda) \ . \tag{5.3}$$

For one of the PMTs receiving m photons of wavelengths $\lambda_1, \cdots, \lambda_m$, the detection probability for that PMT is

$$p(\lambda_1, \cdots, \lambda_m) = 1 - \prod_{i=1}^{m} (1 - p(\lambda_i)) \ , \tag{5.4}$$

where the product term is basically the probability of detecting none of the photons. From these probabilitys $p_1, \cdots, p_s$ for s involved PMTs, the contibuting weigth for a coincidence of order k and the coincidence time window l is

$$w_{k,l} = \begin{cases} \sum_\sigma \prod_{i=1}^{k} p_{\sigma(i)} \prod_{j=k+1}^{s} (1 - p_{\sigma(j)}) & k \leq n \\ 0 & k > n \end{cases} , \tag{5.5}$$

where σ stands for all permutations over the indices. In the end, the weights just summed up to the number of events

$$n_k = \sum_l w_{k,l} \ . \tag{5.6}$$

This leads to the rate of k-fold coincidences

$$\nu_k = \frac{n_k}{t} \tag{5.7}$$

and for the overall coincidence rate including all orders higher or equal than k

$$\nu_{\geq k} = \sum_{i=k}^{\infty} \nu_i \ . \tag{5.8}$$

In the following, the rates already including the background rates are denoted as the total rates, calculated as

$$\nu_{\geq k,\text{total}} = \nu_{\geq k} + \nu_{\geq k,\text{background}} \ . \tag{5.9}$$

5.1.2 Background & Random Coincidences

In general, the effects contributing to the single rate background have a non trivial behaviour, due to spatial inhomogeneity or timedependency. This complexity would lead to different cases, which are needed for taken into account, this would exceed the available project time by far. Therefore the used single rate background just consists of the PMT darkrate (as defined in Equation 5.2) and is calculated as

$$\nu_{\text{single,background}} = \alpha \cdot \nu_{\text{dark}} \ , \tag{5.10}$$

where α is the number of PMTs contributing to the rate. It is $\alpha = 31$ for the overall rates, which is the number of PMTs in the used DOM.

The "backround" in terms of the twofold coincidence rates are the random coincidences, which are calculated as

$$\nu_{\text{random},\mathcal{A}} = \nu^2_{\text{single},\mathcal{A}} \cdot \tau \ , \tag{5.11}$$

for a certain event type $\mathcal{A}$, where $\tau = 10\,\text{ns}$ is the used coincidence time window.

For the single-hit background, meaning the PMT darkrate, this gets $\nu_{\text{random,dark}} = 0.86\,\text{Hz}$, which is neglectable. The random coincidences from ^{40}K decays is $\nu_{\text{random,single}} = 144\,\text{Hz}$, using a single rate value of $\nu_{\text{single,total}} = 120\,\text{kHz}$

per DOM, i.e. 31 PMTs (see Figure 5.1). This is used as the background rate $\nu_{\text{twofold,background}} = \nu_{\text{random,single}}$.

5.2 Simulation Parameters

Due to the limited CPU time in combination with the time consuming GEANT4 implementation, it is obligatory to run the simulation with an optimal choice of its input parameters.

5.2.1 Worldsize

In general the size of the world sphere should be as large as possible to obtain comparable results. This is caused by the simulation world boundary, which removes all particles reaching this boundary. That behaviour is equal to a perfect absorber material and causes a deviation to the real seawater with respect to the contribution of processes happening at larger distances.

A negative consequence of that, the computation time, for gathering the same statistics compared to a smaller world, increases a lot. According to Equation 4.2 the observation time equivalent is indirect proportional to the world volume. This means in case of the used spherical world volume, that $T \propto \frac{1}{r^3}$ decreases very fast. To compensate this, the number of ^{40}K events has to be higher by this factor $\propto r^3$, which increases the computation expenses for the simulation significantly.

The single-hit rate and the twofold coincidence rate as a function of the world size is given in Figure 5.1. For the single-hit rates, large world sizes are needed since the

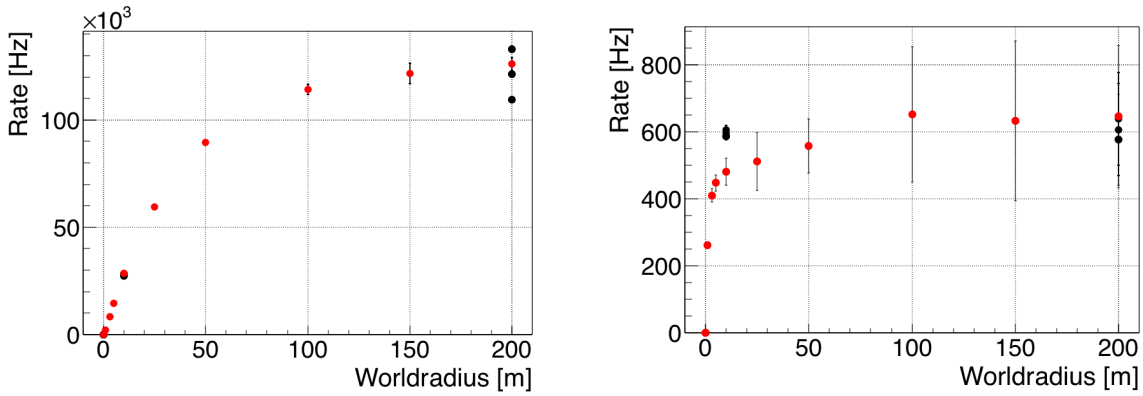

Figure 5.1: Single-hit rates and twofold coincidence rates as a function of the world size. Red markers show the simulation including the absorption length and the black markers excluding it. Error bars show the statistical error.

rate increase starts to diminish at roughly 100 m. Nevertheless, the rates are still growing even at a world radius of 200 m. For the coincidence rates, this flattening effect starts way earlier, at less than 10 m.

Figure 5.2 shows the spatial distribution of the coincident events of different multiplicities. It can be seen that events from all distances shown contribute to the single

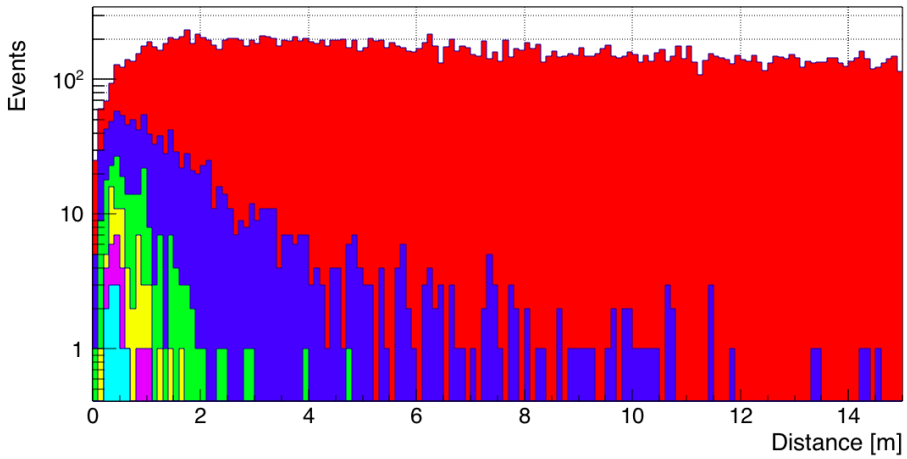

Figure 5.2: Distance of detected ^{40}K-decays depending on the detected coincidence order. Red: single events; Blue: twofold coincidences; Green: threefold coincidences; Yellow: fourfold coincidences; Violett: fivefold coincidences; Cyan: higher orders

rates almost equally, but for the coincidence rates it is limited to a small distance range of a few metres close to the DOM. As it is expected, the overall amount of single events is much larger than coincidence events.

Based on these results, in the further analysis, the sources for the used values is split up. Every single-hit rate data is taken from simulations with a large world radius, which is 200 m in the concrete case. The lower observation time, does not cause negative effects in this case, because the number of received events contributing to the single-hit rate is way higher than for the coincidences.
For the coincidences a world radius of 10 m has been choosen, because for the rate evolution the value is already in range of the convergence value. This is underlined by the event distances in Figure 5.2, which shows, that the contibuting events above 10 m are at least two magnitudes smaller than the peak value.

5.2.2 Simulated vs. Analytic Absorption Length

There are two different ways to deal with the absorption length of water in the simulation. It can be implemented in the simulation directly or set to infinity and

considered after the simulation by taking it into account afterwards. Both approaches should yield similar results but the latter has two important advantages. Since no photons are discarded during the simulation due to absorption, a smaller computing time is needed to accumulate a certain amount of events. In addition when comparing different absorption lengths, the time consuming simulation has not to be repeated.

To verify this proceeding, the spectral distribution and the detection rates are compared for both cases. A comparison of the spectra of the used worldsizes are given in Figure 5.3, which match very well, confirming the similarity of both approaches.

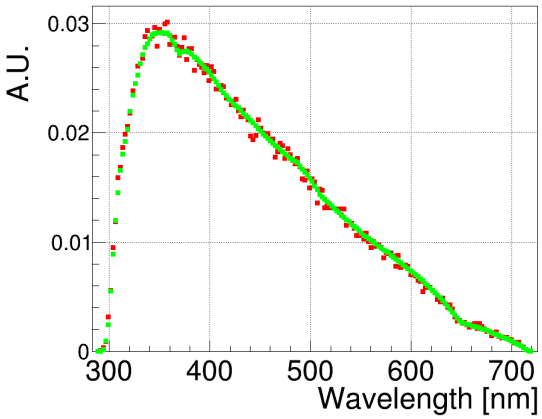

(a) World radius 10 m.

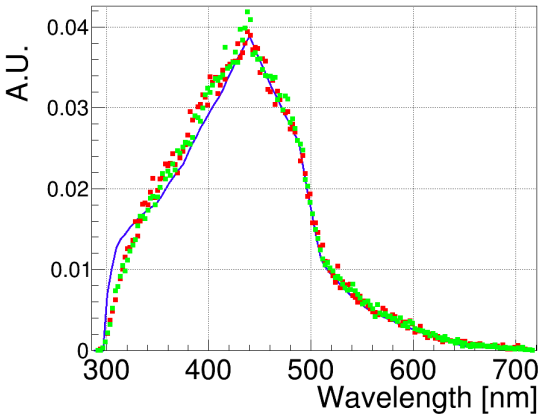

(b) World radius 200 m. The blue line shows the expected absorption spectrum (without scattering) according to appendix A.

Figure 5.3: Comparison of the received spectra from the simulation with explicit absorption (red dots) and analysis (green dots) approach for the used world radii. Due to the different number of entries, the spectra are normalized.

The comparison of the rates was already provided in Figure 5.1, where the red markers label the values of the simulation including the absorption length. The black markers show the rate values for the absorption length considered in the data analysis afterwards.
In this comparison, both approaches deliver comparable results, too, except for a deviation of the twofold coincidence rates at the 10 m world radius. The difference is about $\Delta\nu_{\text{twofold}} \simeq 120\,\text{Hz}$, which can be explained via the random coincidences.
In Figure 5.4 the timespans between the involved photon hits of the coincidence events are drawn. The tail above 1 ns is caused by random coincidences [Her17, fig. 6.9], which are lower by factor 10 for the 10 m sphere with simulated absorption length. This leads to a difference of $\Delta\nu_{\text{twofold}} = 0.9 \cdot \nu_{\text{random}} = 129.6\,\text{Hz}$.

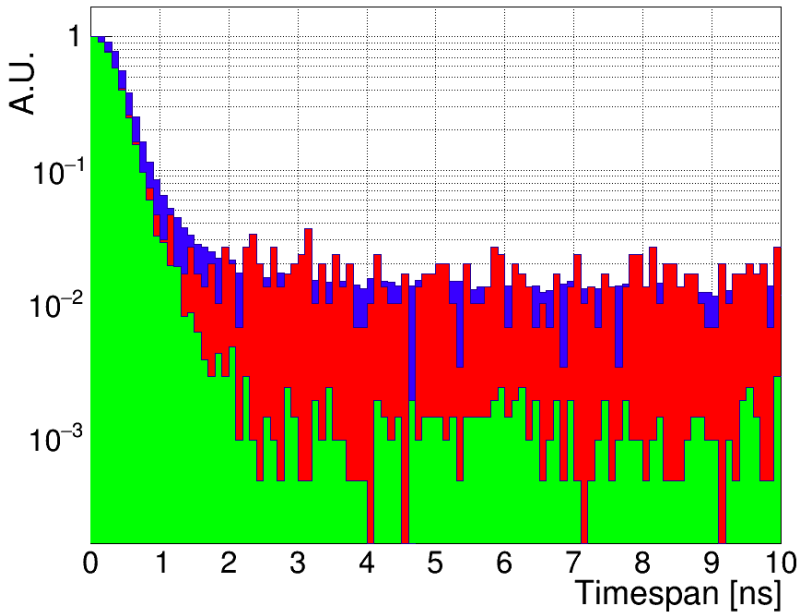

Figure 5.4: Timespan distribution of the contributing events for a twofold coincidence. The included histograms, 10 m simulated absorption length (green), 10 m analytic absorption length (blue) and 200 m simulated absorption length (red), are scaled to their maximum being 1.

5.3 Simulation Characterisation

A characterisation of the simulation enviroment is done for two reasons. The prevention of unexpected behaviour of the simulation enviroment, which would lead to incorrect simulation results. The other reason is the connection to real measurement data, which should support the validity of the simulation results.

5.3.1 Water Properties

The seawater is the key part of the simulation, as the absorption length is the main aspect of this study. Therefore, this part got special attention and it was characterised, even though the code of *nuke4* was not changed with respect to the implementation of the water. The results for the absorption length and the scattering length, which were gathered with the first "White Quasi Laser" setup (see Section 4.3.1), are illustrated in Figure 5.5. While the simulation run for the characterisation of the scattering length, the distribution of the scattering angles was recorded, too. These results are plotted in Figure 5.6.
Regarding the data consistency, the parametrisation of the material (`G4Material`) and the recording of the data (`G4SteppingAction`) has been done via two completely independent objects (see Chapter 4).

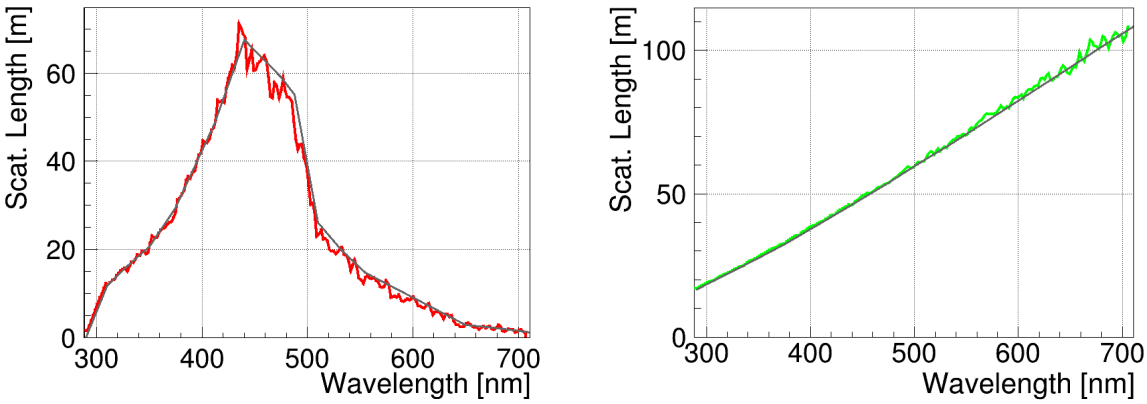

(a) Absorption length.

(b) Scattering length

Figure 5.5: Characterisation results for the absorption and the scattering length in the simulated seawater. For a better comparability the input parameters (given in Figure 2.1) are also plotted in gray.

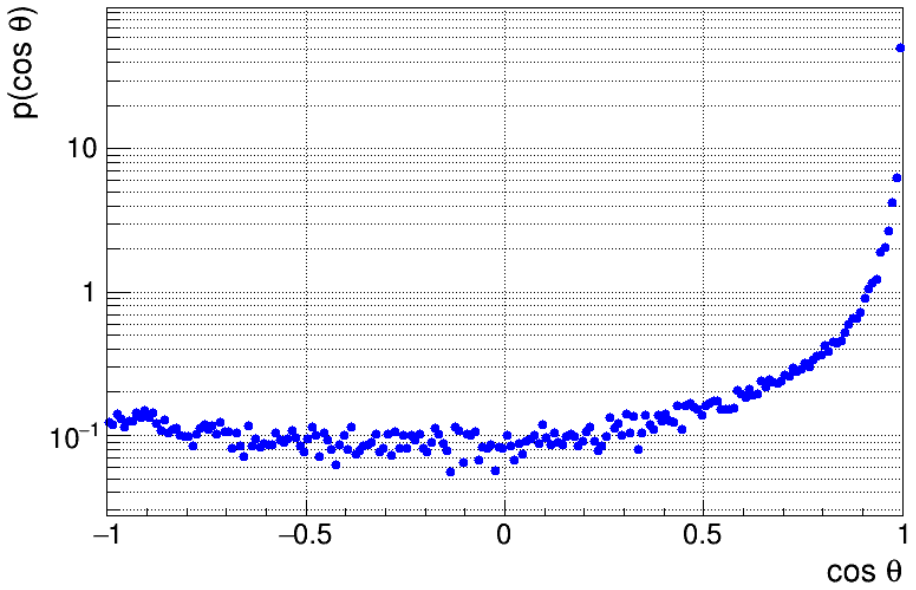

Figure 5.6: Characterisation results for the scattering angle distibution in the simulated seawater for the same exemplary wavelength of 400 nm (as in Figure 2.2).

.

As the Figures 5.5 and 5.6 show, the simulated seawater behaves as expected.

5.3.2 Photon Incident Angular Dependencies

In the rate analysis the QE and CE of the center part of the PMT at perpendicular photon incident are considered for the detection efficiency of a photon hit. As it is known from measurements, the detection efficiency of a PMT also depends on the displacement from the photocathode center and the incident angle of the hitting photon.

The angular distibutions of the incident photons of the analysis and simulated absorption length approaches are given in Figure 5.7. It is plotted over the cosine of the photon angles with respect to the direction the PMT is pointing at. It is expected to be equally distributed between 1 and the opening angle of the PMT on the DOM surface, which is about 0.55 on the used range. This opening angle includes the area covered by the reflector ring around the PMT. Together with the slight different radii of the DOM glass and the photocathode might explain the linear drop and the rebound towards higher angles.

This part of the results was performed in order to get an idea of the distribution and for the possibility of the comparison to later results. A detailed analysis of this angular distribution was not done.

Another interesting aspect of the angular dependency is the reflecting behavior of the reflector rings around the PMT. Due to its curvature this might differ from the properties of a flat mirror.
In Figure 5.9 the spectral distribution integrated over all displacements is given. Towards larger angles, the amount of received photon hits drops like it is expected from Figure 5.8. On the energy axis no major deviation from the uniform distribution of the used “white quasi laser” can be identified. This means for the simulation of the ^{40}K decays, the expected Cherenkov spectrum is not distorted by the reflection.

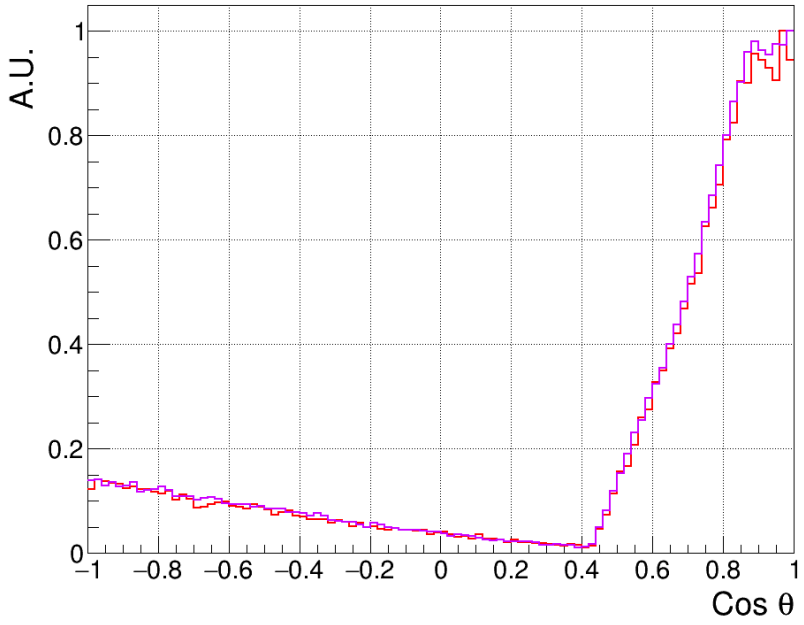

Figure 5.7: Incident photon angle distribution at the photocathode with respect to the PMT normal vector. According to Section 5.2.2, both histograms for the analysed (violet) and the simulated (red) absorption length with world radius 200 m are drawn. The histograms are normalized to their peaks being 1.

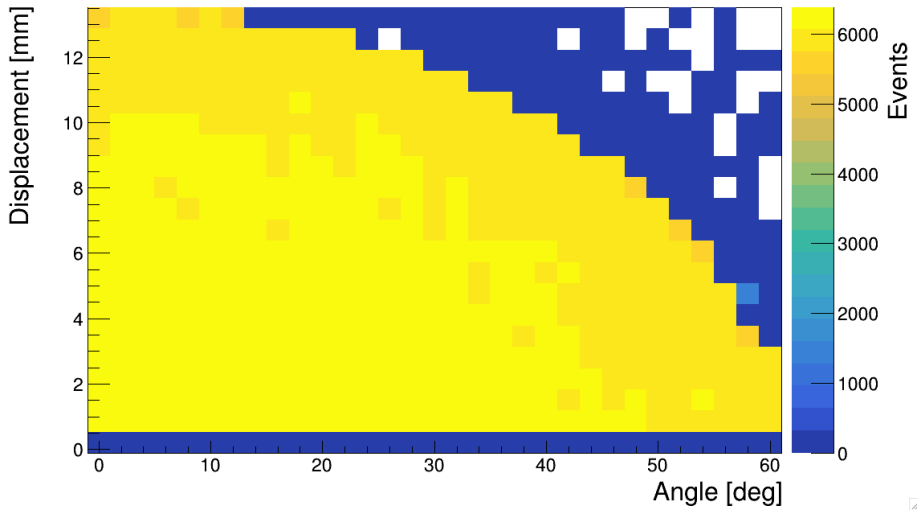

Figure 5.8: Received hits at the photocathode for the second "white quasi laser" setup (Section 4.3.1) illuminating the reflecting PMT ring under a certain angle and a certain distance to the inner rim of the ring.

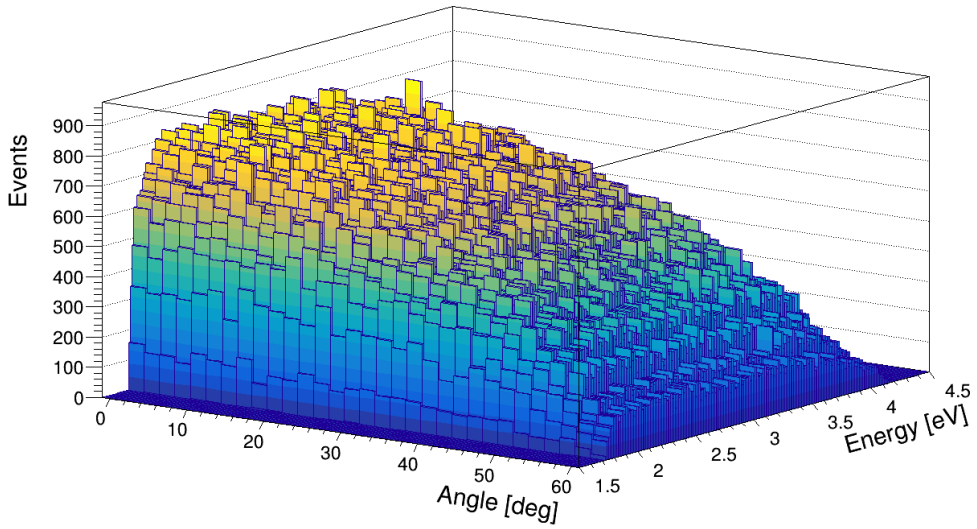

Figure 5.9: Received hits at the photocathode for the second "white quasi laser" setup (Section 4.3.1) illuminating the reflecting PMT ring under a certain angle. It is plotted as a spectral distribution, while the hits are integrated over all displacements from the inner rim of the ring.

5.3.3 Comparison to Detector Data

The comparison to the actual measurement data is done, due to intention of building a bridge from virtual simulation data to the real detector. As the simulation data is also evaluated as detection rates, which is the observable commonly used to analyse the detector data, both can be compared directly.

The single-hit rates might show significant differences, because of effects which were not considered in the simulation, e.g. the darkrate of the PMTs or bioluminescence. Also the limited world size can lead to different results, which is discussed in Section 5.2.1.

A way to get a geometrical information from twofold coincidences, is to split up the total twofold coincidence rate into the twofold coincidence rate for every PMT pair. This analysis with the detector data is given in Figure 5.10a.

As it is expected, the rate increases for more close-by PMTs, because these share a bigger effective detection area for the same solid angle part. The comparison of both plots in Figure 5.10 shows, good agreement between the distributions and total coincidence rate values.

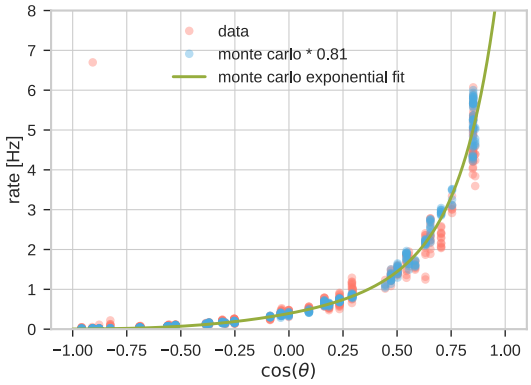

(a) Measurement and *OMGSim* data. Figure taken from [Reu18]

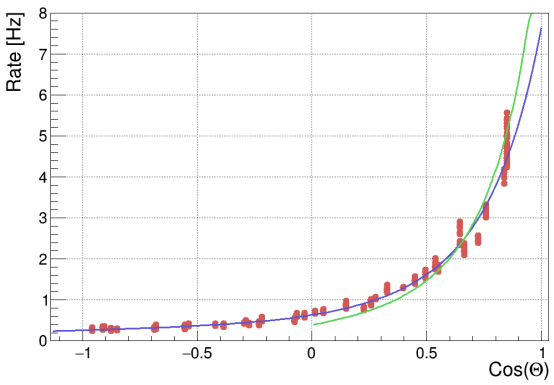

(b) Simulation data. (Green line with fit parameters of figure part a.)

Figure 5.10: Comparison between pairwise coincidence rates of detector data and from simulation data. The rates are plotted for all pairs of PMTs as a function of the cosine of the angle between their pointing directions

5.4 Spectral Rate Distribution

So far, the picture of the environment is more a black and white image, because all photons over the whole wavelength range accounted to the rates. For turning this into a coloured picture, the arrived photons are split into 20 equally spaced wavelength ranges between 290 nm and 710 nm. This emulates a hardware setup with 20 colour filters with perfect transmissivity.

The available data is analysed with respect to different models, which was the reason for the work done in Section 5.2.2. It is most likely that the basic shape of the absorption length distribution in the seawater will not change in general. Therefore the values from the KM3NeT water model are compared to them varied by ±10%(and ±25%).

The results for the different rate types are represented in two different ways. The first one contains the spectral distribution of the rates, whereas in the second graph the relative difference

$$R(\lambda) = \left| \frac{\nu(\lambda) - \nu_{\text{ref}}(\lambda)}{\nu_{\text{ref}}(\lambda)} \right| \tag{5.12}$$

between the models is plotted, which gives a better picture for the comparison. In Equation 5.12 $\nu(\lambda)$ is the compared rate value at wavelength λ, where $\nu_{\text{ref}}(\lambda)$ is the rate value of the referenced model at the same wavelength. In the following,

the referenced rates are for the absorption lengths according to the KM3NeT water model.

5.4.1 Single-hit Rate Picture

In Figure 5.11 the above mentioned spectral distributions for the single-hit rates are provided. The rate variation is approximately linear over the whole wavelength range, except for the last colour filter around 710 nm. This seems to be already a

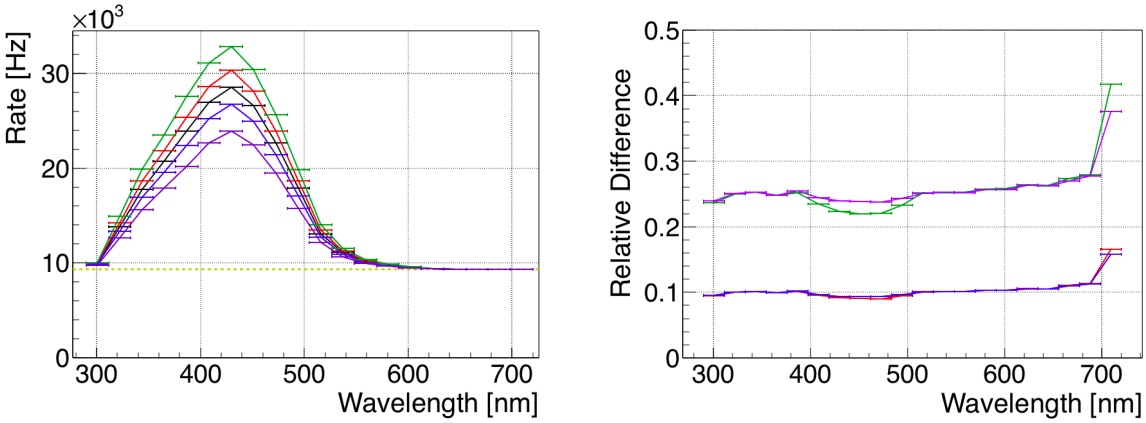

(a) Single-hit rates and the background rate (yellow).

(b) Single-hit rate differences.

Figure 5.11: Spectral single-hit rates for the absorption length distribution according to the KM3NeT water model and it varied by −10% (blue),+10% (red), −25% (violet) and +25% (green). The data points already include the assumed darkrate. The error bars in x direction show the widths of the filters.

very promising result, but the problem of using single-hit rates is the identification of the source. Single-hits also could be caused by the background sources not taken into account, e.g. like bioluminesence, which are not expected to be homogenously distributed and might have a different spectrum.

5.4.2 ^{40}K Coincidence Picture

The identification of the source is less of a problem for ^{40}K coincidences, because the connected events are within a timespan of 1 ns.[1] The coincidence rates of each wavelength range are calculated independently in the way it was outlined in Section 5.1.1. As an additional constraint with respect to a possible hardware solution, just coincidences from PMTs with an opening angle of $\cos\theta > 0.6$ are considered. This

[1] This timing information can be gained from the discussion of Figure 5.4.

emulates a design where neighbouring PMTs are equipped with the same filters.

The results with respect to the coincidences are given in Figure 5.12, which already includes the random coincidences. For an absorption length variation by ±10% the

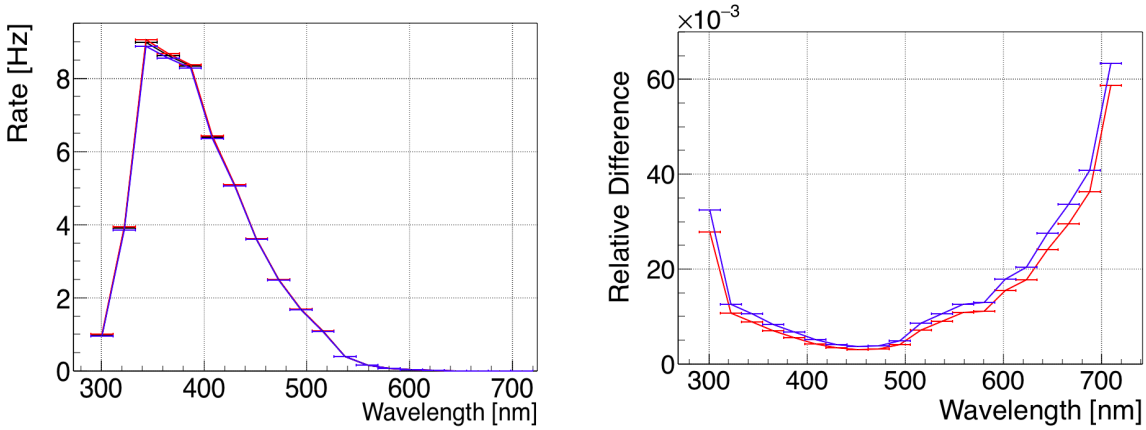

(a) Spectral coincidence rates

(b) Spectral coincidence rate differences

Figure 5.12: Spectral coincidence rates for the absorption length distribution according to the KM3NeT water model and it varied by−10% (blue) and +10% (red).

rate differences are $1-3\%$ for $x < 600\,\text{nm}$.
As it will turn out in Section 5.5, during the detailed discussion of the magnitude of the errors, the measurement duration of the simulation is not long enought for making these coincidence results definite, with respect to the statistical errors.

To underline the order of magnitude of the gathered results regarding the coincidences, an analytic expression for the relative difference can be used for comparison. For this analytic relative difference $\tilde{R}(\lambda)$, it is assumed that the coincdence rates are linear in the exponential factor of Equation 2.1, meaning

$$\nu \propto \exp\left(\frac{d}{L(\lambda)}\right) \quad . \tag{5.13}$$

According to the results of the calculation in appendix A this is not the case in general, but it yields the expression

$$\tilde{R}(\lambda) := \left| \frac{\exp\left(\frac{\langle d_{\text{coincidence}}\rangle}{L(\lambda)}\right)}{\exp\left(\frac{\langle d_{\text{coincidence}}\rangle}{L_{\text{Ref}}(\lambda)}\right)} - 1 \right| \quad . \tag{5.14}$$

The distance of events contributing to the coincidence rate results from Figure 5.2 and has its mean, with respect to all coincidence orders, at

$$\langle d_{\text{coincidence}} \rangle = 2.76\,\text{m} \pm 0.07\ . \tag{5.15}$$

The wavelength dependent reference absorption length $L_{\text{Ref}}(\lambda)$ are the values of the KM3NeT water model. The results for the ±10% variation are plotted in Figure 5.13, which shows a much similar distribution as the simulation results in Figure 5.12b. The more steep slopes at the edges of this plot can be explained via the lower

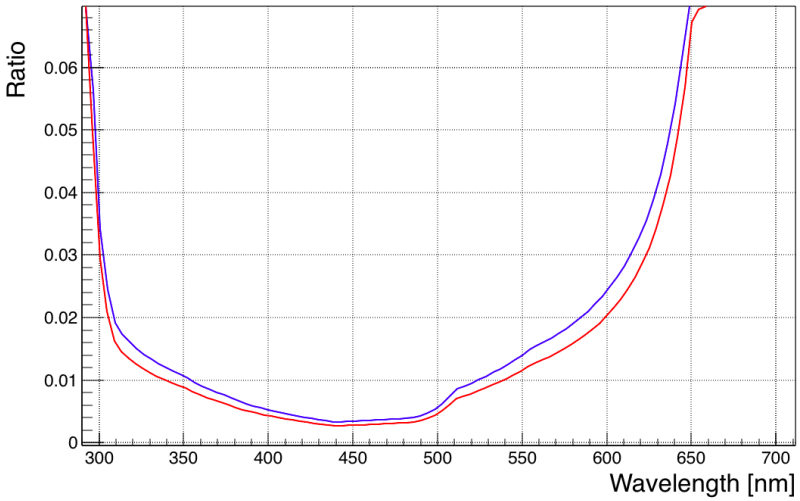

Figure 5.13: Analytic relative differences $\tilde{R}$ as defined in Equation 5.14 for the KM3NeT absorption lengths varied by −10% (blue) and +10% (red).

absorption lengths at these wavelengths, where the assumed linear case does not include higher order terms.

5.5 Statistical and Systematic Errors

In order to resolve the absorption length variation with the desired precision, the statistical and systematic errors for the rate differences have to be considered. Therefore an estimation of both is required, to gather a final assessment with respect to the realisablity of the concept.

The rates are expected to follow a Poisson distribution, assuming the environment conditions are stable, which is the case for the simulation. Thus, the statistical error can be reduced to the required upper limit using a sufficiently long measurement

duration. In this case the relative statistical error is calculated as

$$\Delta_{\text{stat}} R = \frac{\sigma_\nu}{\nu} = \sqrt{\frac{1}{\nu\, T}} \ , \tag{5.16}$$

which can be reshaped to

$$T = \frac{1}{\Delta_{\text{stat}} R^2\, \nu} \ , \tag{5.17}$$

for evaluating the necessary measurement durations. The simulation values, discussed in Section 5.4, are listed together with the resulting measurement durations in Table 5.1. Assuming the variations taking place on much larger time-scales com-

Type	$\min(\Delta_{\text{stat}} R)$	$\max(\nu)$	T	T / PMTs per filter type
single-hit	9.0%	$2.0 \cdot 10^4$ Hz	6.2 ms	0.19 s
coincidences	0.5%	6 Hz	1.9 h	57.4 h

Table 5.1: Estimation of the required measurement durations based on the simulation values. The minimum and maximum is taken with respect to the most important wavelength range between 350 nm and 500 nm.

pared to these measurement durations, the statistical errors are a negligible problem. Thus, the remaining limiting factor for measuring the absorption lengths are the systematic errors of the setup.

The systematic rate error results from the uncertainty with respect to hardware quantities. It is assumed that the systematic error $\Delta_{\text{sys}} p(\lambda)$ is linear in the detection probability $p(\lambda)$:

$$\Delta_{\text{sys}} p(\lambda) = c \cdot p(\lambda) \ . \tag{5.18}$$

This assumption is based on the estimated the systematic error of the QE measurement setup, which was also used to measure the QEs in Figure 2.5.

In the next step, the possibility to receive multiple photons at the PMTs photocathode, which was considered via Equation 5.4, has to be taken into account. Therefore, the actual situation at the photocathode was analysed first, which is given in Figure 5.14. In these histograms, the mean amount of incident photons per photocathode within one coincidence time window is shown. It is obvious, that a single photon hit at the photocathode is the dominant case. Therefore, Equation 5.18 is also used for the general case, meaning

$$\Delta_{\text{sys}} p(\lambda_1, \cdots, \lambda_m) = c \cdot p(\lambda_1, \cdots, \lambda_m) \ . \tag{5.19}$$

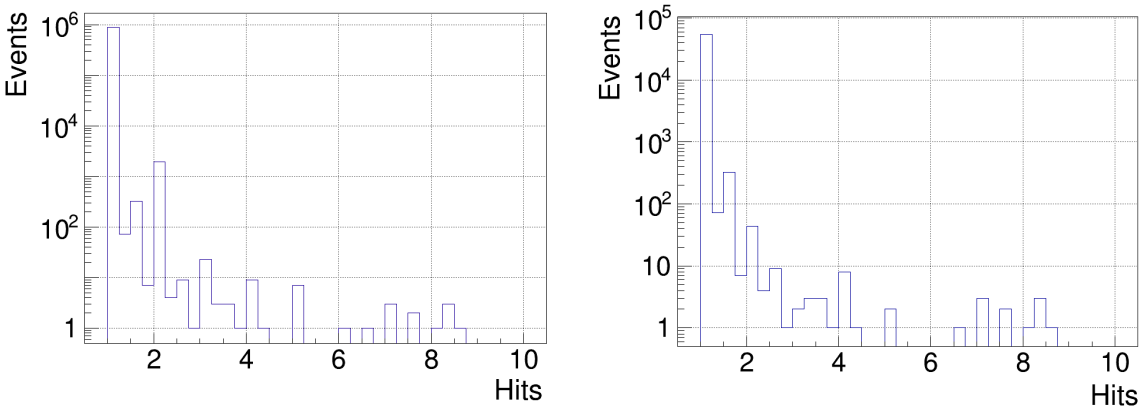

(a) Overall hits at the photocathode. **(b)** Coincidence hits at the photocathode.

Figure 5.14: Average number of received photon hits at one photocathode within one coincidence time window, which is the overall number of photon hits at all PMTs within one coincidence time window divided by the number of involved PMTs.

As the single-hit rate ν_{single} is linear in the detection probability, this should lead to a systematic error of

$$\Delta\nu_{\text{single}} = c \cdot \nu_{\text{single}} \ . \tag{5.20}$$

The total error includes also the error on the background rate, which is the darkrate of the PMTs in the single-hit rate case. As the darkrate of the PMTs should be independent, the total single-hit background error $\Delta\nu_{\text{single,background}}$ for the 31 PMTs is

$$\Delta\nu_{\text{single,background}} = \sqrt{31}\,\Delta\nu_{\text{dark}} \ . \tag{5.21}$$

Finally, the total systematic error for the single-hit rates $\Delta\nu_{\text{single,total}}(\lambda)$ gets

$$\Delta\nu_{\text{single,total}}(\lambda) = \sqrt{c^2 \cdot \nu_{\text{single}}(\lambda)^2 + \Delta\nu^2_{\text{single,background}}} \quad . \tag{5.22}$$

The measurement of the PMT signals is assumed to be independent, which makes the Gaussian error propagation for total coincidence rates in Equation 5.8 applicable.

The detection probability for a coincidence within one coincidence time window $p_{\geq\text{twofold}}$ can also be written as

$$p_{\geq\text{twofold}} = \sum_{i\neq j}^{m} p_i\, p_j \ , \tag{5.23}$$

where m is the number of PMTs, which received a photon hit, and p_i, p_j the detection probabilies for the PMTs. Using the partial derivatives

$$\frac{\partial p_{\geq \text{twofold}}}{\partial p_i} = \sum_{i \neq j} p_j \tag{5.24}$$

the error propagation for the twofold coincidence rates is

$$\Delta p_{\geq \text{twofold}} = \sqrt{\sum_{i=1}^{m} \left(\sum_{i \neq j} p_j \right)^2 \Delta p_i^2} \tag{5.25}$$

$$= \sqrt{\sum_{i=1}^{m} \left(\sum_{i \neq j} p_j \right)^2 c^2 p_i^2} \tag{5.26}$$

$$= c \sqrt{m}\, p_{\text{twofold,total}} \ . \tag{5.27}$$

As these are summed up, the systematic error of the total twofold coincidence rates $\Delta\nu_{\geq \text{twofold}}$ is

$$\Delta\nu_{\geq \text{twofold}} = c \left\langle \sqrt{m} \right\rangle \nu_{\geq \text{twofold}} \quad , \tag{5.28}$$

where $\langle \sqrt{m} \rangle$ is the mean square root of PMTs receiving at least a photon hit within a coincidence time window. According to the simulation this mean value is

$$\langle \sqrt{m} \rangle = 1.44 \pm 0.10 \quad . \tag{5.29}$$

For the systematic error the error terms of the background rate have to be considered, too. Therefore the total systematic error for the twofold rates is

$$\Delta\nu_{\geq \text{twofold,total}} = c \sqrt{\langle \sqrt{m} \rangle^2 \, \nu_{\geq \text{twofold}}(\lambda)^2 + 4\nu_{\text{single,total}}(\lambda)^4 \tau^2} \ . \tag{5.30}$$

Finally, in Figure 5.15 the resulting relative systematic errors

$$\Delta_{\text{sys}} R := \frac{\Delta_{\text{sys}} \nu_{\text{total}}(\lambda)}{\nu_{\text{total}}(\lambda)} \tag{5.31}$$

for the single-hit and the coincidence rates, based on the simulation results for the standard KM3NeT water model, are shown.

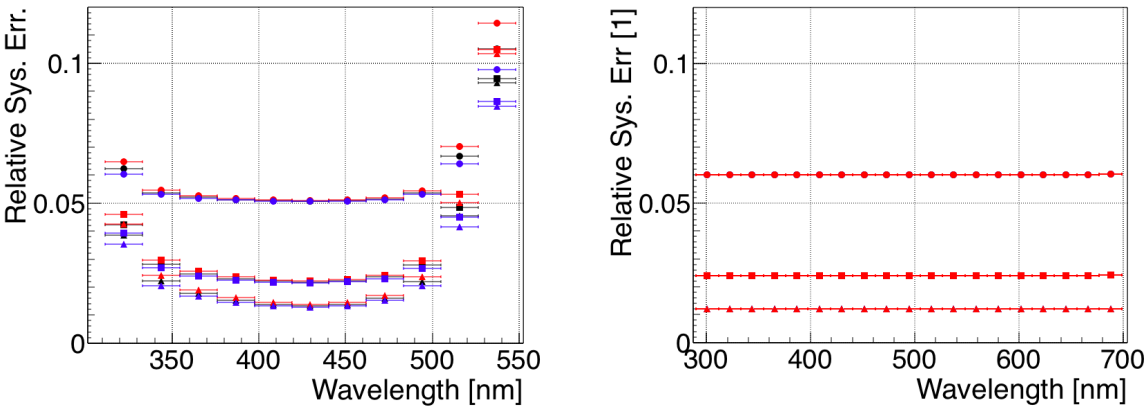

(a) Single-hit rate systematic errors according to Equation 5.22.

(b) Coincidence rate systematic errors according to Equation 5.30.

Figure 5.15: Wavelength dependent relative systematic errors using based on the simulation values. These are given again for the KM3NeT water model (black) and it varied by −10% (blue) and +10% (red). The systematic errors are taken for the cases c to be 1% (triangle), 2% (rectangle) and 5% (circle).

5.6 Results & Discussion

In this final part, the simulation results are combined with the estimated errors in order to reach a final statement on the realisablity.

As there was no general information about the time-dependency of the seawater variations, the statistical errors have to be estimated individually with respect to the available measurement duration and the desired wavelength range. Therefore, the measurement duration is assumend to be long enough and the statistical errors are not taken into account for the final statement.

In order to get a combined picture of the relative rate differences (Equation 5.12) and the relative systematic rate errors (Equation 5.31), the function

$$A_{\pm 10\%}(\lambda) = \frac{\Delta_{\text{sys}}\nu_{\text{Ref}}(\lambda)}{\nu_{\text{Ref}}(\lambda)} \left| \frac{\nu_{\pm 10\%}(\lambda) - \nu_{\text{Ref}}(\lambda)}{\nu_{\text{Ref}}(\lambda)} \right|^{-1} \tag{5.32}$$

$$= \left| \frac{\Delta_{\text{sys}}\nu_{\text{Ref}}(\lambda)}{\nu_{\pm 10\%}(\lambda) - \nu_{\text{Ref}}(\lambda)} \right| \tag{5.33}$$

is defined. If the error at a certain wavelength λ exceeds the rate difference for the reflected variation, the value $A(\lambda)$ rises above the threshold value 1. The results for $A_{\pm 10\%}(\lambda)$, based on the assumed systematic errors from Section 5.5 and the

simulation results, are shown in Figure 5.16.

For the coincidences, $A_{\pm 10\%}(\lambda)$ sinks just under the threshold for the optimistic

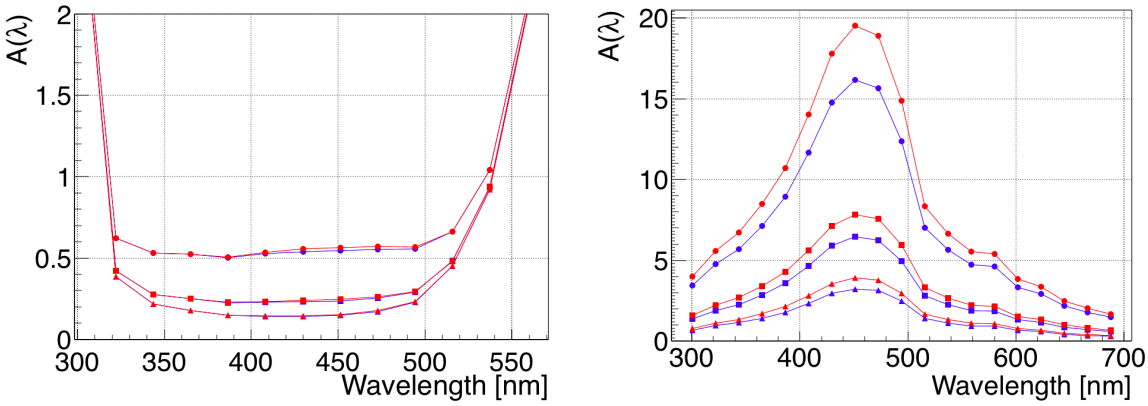

(a) Single-hits. **(b)** Coincidences

Figure 5.16: The results for function $A_{\pm 10\%}(\lambda)$ defined in Equation 5.33. In both plots the KM3NeT water model difference, to itself varied by -10% (blue) and $+10\%$ (red) is shown. The systematic errors are taken for the cases c to be 1% (triangle), 2% (rectangle) and 5% (circle).

case of c being 1%. Even if this would state a realistic scenario, this fall below 1 happens just for short wavelength ranges at the edges of the visible light spectrum, which disqualifies this case nevertheless. All in all, under the given conditions and assumptions, coincidences do not qualify for monitoring the absorption lengths in the seawater for a variation of $\pm 10\%$ or less.

For single-hit rates, the situation is quite different. As Figure 5.16a shows, the value of $A_{\pm 10\%}(\lambda)$ drops under the threshold for all assumed uncertainties c between 310 nm and 520 nm. Therefore this method fulfils the requirements for monitoring the absorption lengths in the seawater for a variation of $\pm 10\%$ or less for all assumed values for c.

Another important scenario for the systematic errors of the single-hit rates is the darkrate of the PMTs being correlated. The PMTs are under the influence of the same environmental conditions, which could correlate their measurement rate. In addition crosstalk between the PMTs can contribute to the PMTs darkrate being correlated. Equation 5.21 is therefore modified to

$$\Delta\nu_{\text{single,background}} = 31\,\Delta\nu_{\text{dark}}\ , \tag{5.34}$$

which means the systematic error increases linearly with the amount of used PMTs. The results for this modified assumption applied are shown in Figure 5.17. As

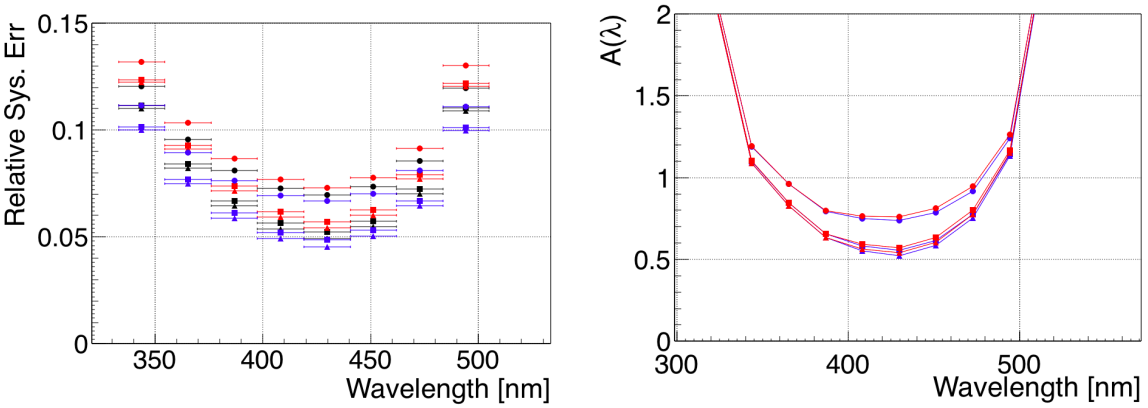

(a) Single-hit rate systematic errors.

(b) Single-hit rate results for function $A(\lambda)$.

Figure 5.17: The results for systematic errors and the function $A_{\pm 10\%}(\lambda)$ defined in Equation 5.33. The results are shown for a KM3NeT water model differencef varied by -10% (blue) and $+10\%$ (red) and the systematic errors are taken for the cases c to be 1% (triangle), 2% (rectangle) and 5% (circle).

expected, the relative systematic errors are higher for all assumed values for c with its minimum ($c = 1\%$) around 5%. For resolving the variation of $\pm 10\%$, this is still enough, which can be deduced from Figure 5.17b. The wavelength range of values for $A_{\pm 10\%}(\lambda) < 1$ is smaller than in the case of uncorrelated dark rate errors.

The upper limits for c and $\Delta\nu_{\text{background}}$ for one PMT, such that $\exists\lambda : \min(A_{\pm 10\%}(\lambda)) \leq 1$, are:

- $\max(c) = 0.1$ for $\nu_{\text{darkrate}} = 0$,
- $\max(\Delta\nu_{\text{background}}) = 58\,\text{Hz}$ for the correlated case of Eq. 5.34 and $c = 0$ and
- $\max(\Delta\nu_{\text{background}}) = 316\,\text{Hz}$ for the uncorrelated case of Eq. 5.21 and $c = 0$,

where the wavelength range of the colour filter is around $430\,\text{nm} \pm 11\,\text{nm}$. Due to the linear behaviour in the single-hit rate case, which was deduced from Figure 5.11b, the limits for resolving an absorption length variation of $\pm 1\%$ is just:

- $\max(c) = 0.01$ for $\nu_{\text{darkrate}} = 0$,
- $\max(\Delta\nu_{\text{background}}) = 5.8\,\text{Hz}$ for the correlated case of Eq. 5.34 and $c = 0$ and
- $\max(\Delta\nu_{\text{background}}) = 31.6\,\text{Hz}$ for the uncorrelated case of Eq. 5.21 and $c = 0$.

As this looks very promising, the single-hit rates seem to be the predestined way of doing the monitoring. But this result has always to be considered in context of the environmental conditions of the simulation and the used assumptions. In this

picture no bioluminesence and other processes were taken into account for single-hit rate background, but these are expected to have significant influence on the results for single-hit rates. Also the usage of a different amount of colour filters with realistic behaviour has to be taken into account, too.

6 Conclusion & Outlook

The starting point of this project was the adoption of the *nuke4* implementation and its update to the latest geometry. With the characterisation and the comparison to the detector data, *nuke4* is well prepared for further usage in other projects.

In the main part of the project, it was dealt with the spectral analysis of the detection rates with respect to the wavelength dependent photon absorption length in deep-sea water. Along with the estimated systematic errors in the last part, the single rates might be suitable for measure and monitoring the absorption lengths.
For resolving an absorption length variation of $\pm 1\%$ with the single-hit rates, the error on the detection efficiency has to be maximally 1%. The systematic error of the background rate for a single PMT has to be less than 5.78 Hz (31.6 Hz) for the assumption that the overall background of the PMTs is correlated (uncorrelated). These values were gathered for the wavelength range of 22 nm around $\lambda = 430\,\text{nm}$.
The downside of this method is the influence of other sources, e.g. bioluminescence, to the background rate, which makes it difficult to realise.
The coincidence rates do have less of those influences, but the detected ^{40}K events are to close to the DOM, which leads to very weak variations in the spectral rates. Based on the estimated systematic errors and comparatively long measurement duration, these variations are assessed of being too weak.

During the project time a lot of additional ideas came up for advancing the basic concept. For example atmospheric muons could be used as background source or a more detailed review of the single rates could be done. Due to the limited time, these ideas could not be followed up, but will be looked into in the future. Beside these conceptional improvements, a more detailed consideration of the hardware properties and a comparison to other data, e.g. from the *OMGSim* implementation [Hug16], is also left to do.

Appendix

A Analytic Spectral Model

In order to get an idea of the incident photon spectrum, an approximate distribution without scattering was estimated. First, the notation used in the calculations is introduced:

$I_{\mathrm{DOM}}(\lambda)$ $\equiv$ Wavelength dependent intensity at the DOM surface.
A $\equiv$ ^{40}K activity in the seawater, which is $A = 13.75\,\mathrm{kBq}$.
$E(\lambda)$ $\equiv$ Mean spectral energy emitted via cherenkov radiation after a decay of one ^{40}K atom.
$S(\lambda)$ $\equiv$ Spectral power density of a ^{40}K decay, which is basically: $S(\lambda) = A \cdot E(\lambda)$.
$\alpha(r)$ $\equiv$ Arbitrary parameter used for simplifying the expressions later on.
$L(\lambda)$ $\equiv$ Absorption length.

As a single ^{40}K decay is assumend to be pointlike lightsource (see section 2.3), the cherenkov lights is emitted isotropically. Therefore the spatial angle part, which is "visible" for the DOM, has a distance dependency

$$\tilde{\Omega}(r) = 2\pi \, \sin\left(\arctan\left(\frac{r_{\mathrm{DOM}}}{r}\right)\right) \tag{1}$$

$$= \frac{2\pi \, \alpha(r)}{\sqrt{\alpha(r)^2 + 1}} \; . \tag{2}$$

For large distances, which is the dominant contribution for the integral, this $\tilde{\Omega}(r)$ is approximately

$$\tilde{\Omega}(r) \approx 2\pi \, r \cdot r_{\mathrm{DOM}} \; . \tag{3}$$

Now the wanted expression for the spectral intensity can be written as an integral

$$I_{\mathrm{DOM}}(\lambda) = \frac{1}{4\pi r_{\mathrm{DOM}}^2} \int_{\Omega} \int_{r_{\mathrm{DOM}}}^{\infty} r^2 \, dr \, d\Omega \exp\left(-\frac{r}{L(\lambda)}\right) S(\lambda)\tilde{\Omega}(r) \tag{4}$$

$$= S(\lambda)\frac{2\pi}{r_{\mathrm{DOM}}} \int_{r_{\mathrm{DOM}}}^{\infty} r^3 \, dr \exp\left(-\frac{r}{L(\lambda)}\right) \ . \tag{5}$$

This integral can be solved using the Feynman-trick

$$I_{\mathrm{DOM}}(\lambda) = \frac{2\pi S(\lambda)}{r_{\mathrm{DOM}}} \left[-L(\lambda)\exp\left(-\frac{r}{L(\lambda)}\right)\left(6L(\lambda)^3 + 6L(\lambda)^2 r + 3L(\lambda)r^2 + r^3\right)\right]_{r_{\mathrm{DOM}}}^{\infty} \tag{6}$$

$$= \frac{2\pi S(\lambda)L(\lambda)}{r_{\mathrm{DOM}}} \exp\left(-\frac{r}{L(\lambda)}\right)\left(6L(\lambda)^3 + 6L(\lambda)^2 r_{\mathrm{DOM}} + 3L(\lambda)r_{\mathrm{DOM}}^2 + r_{\mathrm{DOM}}^3\right) \tag{7}$$

This expression is used as fit function for the fit in figure 5.11b, which is scaled to arbitrary units. Therefore the spectral power density $S(\lambda)$ is set to

$$S(\lambda) = \frac{a}{\lambda^2} \tag{8}$$

with a being a free fit parameter in order to scale the function.

B Simulation Run Parameters

In the tables B.1 and B.2 an overview of the number of used events and the related measurement time equivalent T_{sim} of the underlying simulations for the results in chapter 5 is provided.

World radius	**World volume**	**Placed ^{40}K ions**	T_{sim}
1 m	$4.2\,\text{m}^3$	$1.25 \cdot 10^6$	21.7 s
3 m	$1.1 \cdot 10^2\,\text{m}^3$	$8.33 \cdot 10^6$	5.40 s
5 m	$5.2 \cdot 10^2\,\text{m}^3$	$3.12 \cdot 10^7$	4.34 s
10 m	$4.2 \cdot 10^3\,\text{m}^3$	$5.00 \cdot 10^7$	0.87 s
25 m	$6.5 \cdot 10^4\,\text{m}^3$	$5.86 \cdot 10^8$	0.65 s
50 m	$5.2 \cdot 10^5\,\text{m}^3$	$7.00 \cdot 10^9$	0.97 s
100 m	$4.2 \cdot 10^6\,\text{m}^3$	$7.00 \cdot 10^9$	0.12 s
150 m	$1.4 \cdot 10^7\,\text{m}^3$	$7.00 \cdot 10^9$	0.04 s
200 m	$3.4 \cdot 10^7\,\text{m}^3$	$5.00 \cdot 10^{10}$	0.11 s

Table B.1: Run details of the underlying simulations including the absorption length model.

World radius	**World volume**	**Placed ^{40}K ions**	T_{sim}
10 m	$4.2 \cdot 10^3\,\text{m}^3$	$2.40 \cdot 10^{10}$	415.58 s
200 m	$3.4 \cdot 10^7\,\text{m}^3$	$6.02 \cdot 10^{10}$	0.13 s

Table B.2: Run details of the underlying simulations without the absorption length model.

Bibliography

[AM16] S Adrián-Martínez. et al. *Letter of intent for KM3NeT 2.0* Journal of Physics G: Nuclear and Particle Physics. 43(8):084001, 2016. URL: `http://stacks.iop.org/0954-3899/43/i=8/a=084001`.

[Bru99] Jürgen Brunner. *Simulation of ^{40}K signals*. ANTARES internal note (ANTARES-Site/1999-002), 1999.

[FB92] L. Fülöp and T. Biró. *Cherenkov radiation spectrum* International Journal of Theoretical Physics. 31(Issue 1):pp 61–74, January 1992.

[Her17] Björn Herold. *Simulation and Measurement of Optical Background in the Deep Sea Using a Multi-PMT Optical Module*. PhD thesis, Friedrich-Alexander-Universität Erlangen-Nürnberg (FAU), 2017.

[Hof17] Jannik Hofestädt. *Measuring the neutrino mass hierarchy with the future KM3NeT/ORCA detector*. PhD thesis, Friedrich-Alexander-Universität Erlangen-Nürnberg (FAU), 2017.

[Hor06] A. Horvath. *The geometry of the Cherenkov radiation.* [online]. March 2006. URL: `https://commons.wikimedia.org/wiki/File:Cherenkov.svg` [cited 2018-01-02].

[Hug16] Christophe M. F. Hugon. *GEANT4 simulation of optical modules in neutrino telescopes*. *PoS*, ICRC2015:1106, 2016.

[int14] *Detector simulations for KM3NeT*. KM3NeT internal note (KM3NeT_SIM_2014_001), June 2014.

[JH15] Clancy W. James and Jannik Hofestädt. *Ice and water optical properties*. KM3NeT interal note (KM3NeT_SIM_015_001), 2015.

[Kri14] J. Krieger. *Scheme of a Photomultiplier Tube (PMT) in English* [online]. December 2014. URL: `https://commons.wikimedia.org/wiki/File:Photomultiplier_schema_en.png` [cited 2017-04-26].

[Nie50] Alfred O. Nier. *A Redeterrnination of the Relative Abundances of the Isotopes of Carbon, Nitrogen, Oxygen, Argon, and Potassium* Physical Review Journals. 77(6):789, March 1950.

[Reu18] J. Reubelt. *Hardware studies, in-situ prototype calibration and data analysis of the novel multi-PMT digital optical module for the KM3NeT neutrino telescope (in preparation).* PhD thesis, Friedrich-Alexander Universität Erlangen-Nürnberg, 2018.

[url17] Website GEANT4, 12 2017. URL: `http://geant4.cern.ch` [cited 2017-12-24].

[url18a] Collaboration Website KM3NeT, 2018. URL: `http://www.km3net.org` [cited 2018-02-14].

[url18b] Live chart of nuclides [online]. 2018. URL: `https://www-nds.iaea.org/relnsd/vcharthtml/VChartHTML.html` [cited 2018-01-05].

Danksagungen

An erster Stelle möchte ich mich bei Uli Katz bedanken für die Möglichkeit diese Bachelorarbeit an seinem Lehrstuhl anzufertigen. Mein Dank gilt natürlich auch der KM3NeT-Gruppe und insbesondere Oleg Kalekin, Jannik Hofestädt und Jonas Reubelt für die fachliche Unterstützung und die viele dafür investierte Zeit.
Ein besonderer Dank geht an meine Eltern, meine Schwester Kathrin, sowie Werner und Dagi, die mich in allen Phasen meiner Ausbildung in allen Belangen uneingeschränkt unterstützt haben und mir damit in besonderer Weise mein Studium ermöglicht haben.
Wer ebenso nicht unerwähnt bleiben sollte, sind meine Freunde beim Eishockey und die „Laufer-Connection“, durch die ich zur rechten Zeit ein wenig Zerstreuung gefunden habe, um mit neuer Motivation wieder an die Arbeit zu gehen.

Erklärung

Hiermit bestätige ich, dass ich diese Arbeit selbstständig und nur unter Verwendung der angegebenen Hilfsmittel angefertigt habe.

Erlangen, den 20. Februar 2018

Johannes Schumann